PNAS RESEARCH ARTICLE | BIOPHYSICS AND COMPUTATIONAL BIOLOGY
NEUROSCIENCE

Multicolor photoreactions of the red light–activated channelrhodopsin Chrimson

Johannes Vierock[a,b,1,2], Joel C. D. Kaufmann[c,1], Lukas Faiß[a,d,1], Linda Tillert[a,b], Benjamin S. Krause[b], Paul Fischer[b], Thi Bich Thao Nguyen[b], Dietmar Schmitz[a,d], Benjamin R. Rost[a,d], Franz Bartl[c], and Peter Hegemann[b,2]

Affiliations are included on p. 10.

Contributed by Peter Hegemann; received May 30, 2025; accepted November 18, 2025; reviewed by Leonid S. Brown, Adam E. Cohen, Elena G. Govorunova, and Botond Roska

Channelrhodopsins are light-gated ion channels that are used in modern neurosciences for the precise control of cellular ion fluxes by light. With a peak absorption at 585 nm, Chrimson is the most red-shifted cation-conducting ChR. It is frequently employed in multicolor experiments alongside blue light–sensitive optogenetic tools and is so far the only light-gated ion channel successfully applied in human vision restoration. However, its photoresponses to different wavelengths have not been thoroughly characterized. In this study, we identify multiple interconvertible dark states of Chrimson with distinct absorption and photokinetic properties. Combining electrophysiology and spectroscopy with optogenetic experiments in neurons, we unveil that this dark state heterogeneity is based on distinct protonation dynamics of the counterion complex and alternative retinal isomerization. In neurons, prolonged red illumination reduces Chrimson's red light sensitivity, which is reflected by a blue shift of the action spectrum. Blue light pulses reverse this shift and increase the excitability in subsequent red-light flashes. This understanding of wavelength-dependent photoreactions in Chrimson will improve the design of multicolor optogenetic experiments and inform strategies for optimizing Chrimson for therapeutic applications.

channelrhodopsins | optogenetics | Chrimson | FTIR spectroscopy | retinal prosthesis

Channelrhodopsins (ChRs) are light-gated ion channels that have become valuable research tools in modern neurosciences (1) to control genetically targeted cells with light (2). Red light–activatable ChRs are of particular interest for these optogenetic applications because red light penetrates deeper into tissue and is less cytotoxic than blue or green light (3). The most red-shifted cation-conducting ChR is Chrimson from *Chlamydomonas noctigama*, which has a peak sensitivity at 585 nm (4). This is a 40 nm red-shift in comparison to other red light–sensitive ChRs, such as ChRmine or the Volvox ChR derivatives C1V1 and ReaChR (5–8). Spectrally well separated, Chrimson is often combined with blue light–sensitive tools, such as inhibitory opsins and/or Ca^{2+} sensors, for bidirectional optogenetic control of neuronal activity and use in all-optical experiments (9–11). Furthermore, in *Drosophila* Chrimson can be activated with colors outside the operational range of their native photoreceptors (12, 13). Recently, the fast variant f-Chrimson was identified as a promising candidate for optogenetic restoration of auditory function (14), while the alternative variant ChrimsonR was reported to restore basic visual perception in a blind patient suffering from retinitis pigmentosa (15), making Chrimson the first ChR successfully translated into a clinical application.

Previous studies have investigated the proton conductance, red light absorption, and early photoreactions of Chrimson, and provided a high-resolution crystal structure of the closed state (Fig. 1*A*) (16–19). At neutral pH, photocurrents of Chrimson are primarily carried by protons, while larger cations, such as Na^+, Ca^{2+}, and Gdm^+, are poorly or not at all conducted. Protons likely pass through the pore along a chain of conserved glutamic acids and low water content which confer both a high proton conductance and selectivity (16). The orientation and hydrogen bonding of these glutamates differ from those in other ChRs, forming an additional pore constriction in the extracellular half-channel previously described as the outer gate, which in the dark, occludes the putative ion conducting pathway from the extracellular bulk phase to the protonated retinal Schiff base ($RSBH^+$) (18). Protonation of the counterion Glu165 adjacent to the $RSBH^+$ results in an active site that only weakly stabilizes the electronic ground state of the retinal Schiff base through the more distant counterion D295, thereby reducing the opsin shift and promoting red light absorption (Fig. 1*A* inset) (16–18). Upon short flash stimulation, channel opening follows distinct reaction trajectories depending on the illumination color (17, 19). However, photoresponses of Chrimson to prolonged or

Significance

Optogenetics enables light control of specific cell types by expressing light-modulated channels and enzymes. Red-light-activated ion channels are of special interest, as red light penetrates deeper into brain tissue and allows multicolor light control in combination with blue-shifted channels and sensors. Chrimson is the most red-shifted cation-conducting channelrhodopsin frequently used in living organisms, and the first rhodopsin successfully applied to restore vision in a blind patient. However, its wavelength-dependent photoreactions and light adaptation remain poorly understood. Using UV/Vis and FTIR spectroscopy, electrophysiology, and optogenetics in neurons, we show that Chrimson exists in multiple interconvertible dark states with distinct absorption properties, kinetics, and ion conductance. These insights advance the interpretation of Chrimson-based multicolor experiments and guide illumination protocols for clinical applications.

[1]J.V., J.C.D.K., and L.F. contributed equally to this work.

[2]To whom correspondence may be addressed. Email: johannes.vierock@charite.de or hegemann@hu-berlin.de.

This article contains supporting information online at https://www.pnas.org/lookup/suppl/doi:10.1073/pnas.2513375122/-/DCSupplemental.

Published December 22, 2025.

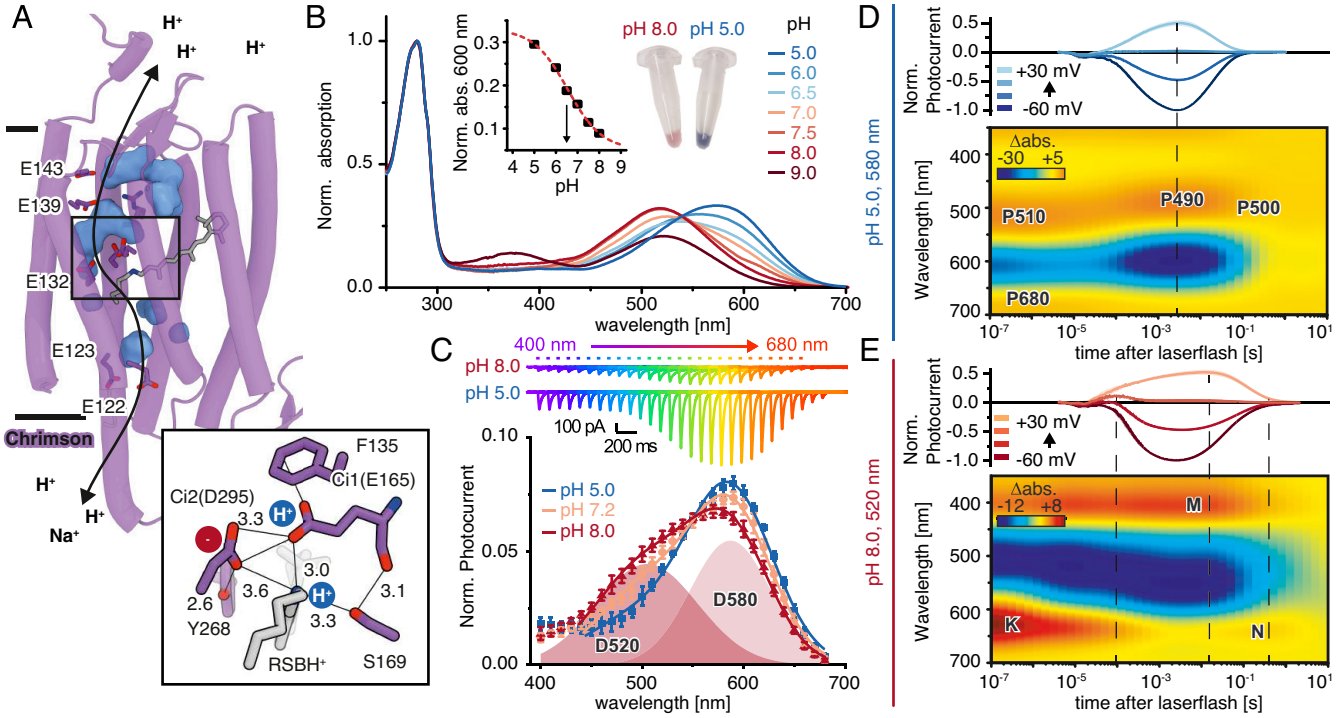

Fig. 1. pH-dependent photocycles of Chrimson. (*A*) C1Chrimson structure (18) with intracellular cavities calculated with Hollow in blue (24) and the putative proton pathway marked by a black arrow. *Inset*: Protonated $RSBH^+$ of Chrimson and its counterion complex with protonated Glu165, Phe135, and deprotonated Asp295 (putative hydrogen bonds as black lines with calculated distances in the dark). (*B*) Absorption spectra of *Cs*Chrimson at different pH and normalized to 280 nm absorption. *Inset Left*: Normalized absorption at 600 nm with a black arrow marking the pKa value of the pH transition. Chrimson absorption at pH 9 was not included because of RSBH+ deprotonation. *Inset Right*: Purified CsChrimson in detergent at pH 5 and 8. (*C*) *Top*: Representative photocurrents of *Cs*Chrimson expressed in HEK293 and illuminated by 10 ms light of different wavelengths but equal photon count at −60 mV and $pH_{e,i}$ 8 or $pH_{e,i}$ 5. *Bottom*: Corresponding action spectra at different symmetric intra- and extracellular pH values (mean ± SD; n = 6 to 10) and fitted at pH 7.2 and pH 8.0 by the sum of two Gaussian distributions representing D520 and D580 and displayed as red surfaces below the curves. All action spectra were normalized for an equal cumulated sensitivity in between 300 and 700 nm. (*D*) *Top:* Normalized single turnover photocurrent recordings of CsChrimson after 7 ns 580 nm laser excitation at different voltages and $pH_{i/e}$ 5.0 (Photocurrents were normalized to their maximal amplitude at −60 mV, averaged for different cells and displayed as Mean ± SE; n = 4 to 6). *Bottom*: Flash photolysis measurements of CsChrimson at pH 5.0 following 580 nm excitation. (*E*) Same as *D* but with 520 nm excitation and $pH_{e,i}$ 8.0.

repetitive illumination remain largely unexplored, despite the significant impact of such protocols on the photocurrents of other ChRs. For instance, ChR2 from *Chlamydomonas reinhardtii* exhibits branching of the photocycle and alternative C15=N *anti-syn* retinal isomerization, which leads to changes in conductance and ion selectivity during prolonged illumination (20, 21). In Mermaid ChRs and a number of cryptophyte ChRs, accumulation of late nonconducting photocycle intermediates results in an almost complete suppression of photocurrents in bright continuous light (22, 23).

In this study, we specifically investigate the phototransitions of Chrimson in response to different illumination colors and durations. Using a combination of stationary and time-resolved single turn-over electrophysiology, as well as UV–Vis and FTIR-difference spectroscopy, we demonstrate that the conformational changes leading to channel opening in Chrimson are small in comparison to other ChRs and unveil an equilibrium of different metastable dark states that are populated depending on extracellular pH and previous illumination history. This color-dependent photoconversion alters Chrimson-mediated depolarization in neurons affecting both the success rate of light-triggered action potentials (APs) and the amplitude of light-evoked transmitter release, which holds important implications for the use of Chrimson in multicolor applications.

Results

pH-Dependent Photocycles of Chrimson. For a comprehensive analysis of channel gating and molecular phototransitions of Chrimson in response to different colors of light, we expressed the targeting-enhanced *Cs*Chrimson variant (Chrimson with N terminus of *Chloromonas subdivisa* ChR) in HEK293 and ND7/23 cells for whole-cell voltage-clamp recordings and purified it from *Pichia pastoris* for complementary spectroscopic characterization.

As previously observed for other Chrimson variants, pH titration of detergent-solubilized CsChrimson confirmed a pronounced shift in peak absorption from 582 nm at pH 5 to 520 nm at pH 8 (17, 18) (Fig. 1*B* and *SI Appendix*, Fig. S1). This color shift had been associated with deprotonation of the first counterion E165 that occurs in CsChrimson with a pK_a value of ~6.5 (Fig. 1*B* and *SI Appendix*, Fig. S1 *B*, *Inset*), which is slightly below the one for Chrimson WT [pK_a 7.4 (17)] or the crystallized N-terminal chimera C1Chrimson [$pK_a > 7.0$ (18)]. At pH 5, the photocurrent action spectrum closely matched the protein absorption spectrum, measured at the same pH (Fig. 1 *B* and *C*). In contrast, at neutral and alkaline pH, the action spectrum was broader and less blue-shifted than expected. Here, both the action and the absorption spectra are best explained by a mixture of both pH-dependent dark states, D520 and D580, each contributing to the overall photocurrent. Within the cellular membrane environment, photocurrents originating from D580 dominate, but, responses to blue and green light increase at positive voltages (*SI Appendix*, Fig. S1 *A* and *D*), showing how different parameters influence the D520/D580 equilibrium.

Individual activation of the two pH-dependent dark states by ns-laser pulses results in distinct photointermediates and open states, as determined by time-resolved absorption measurements and matched single turnover electrical recordings (Fig. 1 *D* and *E*).

At pH 5.0, photocurrents rise and decay within milliseconds, in parallel with the appearance of the blue-shifted photointermediate P490, which represents the open state (Fig. 1*D*). P490 forms without prior deprotonation of the retinal Shiff base (RSB), as no preceding absorption increase in the UV is observed (17, 19). Interestingly, photocurrents rise slightly faster following green light excitation than after red light excitation, confirming distinct reaction pathways for D580 activation and supporting previous observations (19) (*SI Appendix*, Fig. S2). At pH 8.0, channel opening is strongly biphasic and delayed (Fig. 1*E* and *SI Appendix*, Fig. S2 *B* and *C*). The fast kinetic component resembles that observed at pH 5, whereas the slow component leads to full channel opening only 10 ms after laser excitation and temporally correlates with the late M- and N-states of the alkaline photocycle, similar to what has been observed in other ChRs (21, 25). Notably, channel opening at alkaline pH is preceded by a brief outward-directed charge transfer—most clearly observed in the absence of an electrochemical driving force at 0 mV—that peaks at 50 to 100 µs (Fig. 1*E* and *SI Appendix*, Fig. S2*B*) and temporally coincides with M-state formation and the associated deprotonation of the $RSBH^+$. This charge transfer is not detected at acidic pH (Fig. 1*E* and *SI Appendix*, Fig. S2*B*), where none of both processes appears to be required for channel opening.

Light Adaptation of Chrimson. Next, we addressed photoresponses of Chrimson in response to longer illumination pulses. In whole-cell patch-clamp recordings, high intracellular HEPES concentrations were applied via the patch pipette to prevent transient intracellular pH changes that could otherwise complicate the interpretation of the recorded photoresponses (16) (Fig. 2*A*). With sufficient intracellular buffering, photocurrents of Chrimson remain fully stable and showed only negligible inactivation (Fig. 2 *B* (*Top*) and *C*). Accordingly, Chrimson displayed no transient peak currents even after extended dark periods, as typically observed in other ChRs.

However, a remarkable change of the photocurrents was observed following illumination with UV/blue light (Fig. 2 *B*, *Bottom*). After 1 s of 400 nm light exposure, the subsequent, red-induced photocurrent transiently increased by 33 ± 12% at 600 nm and 380 ± 50% at 650 nm (Fig. 2 *B* and *C*). Intriguingly, the duration of the dark period between UV and red-light pulses had no effect on photocurrent amplitude or the extent of its increase (Fig. 2 *D* (*Bottom*) and *E*), suggesting the presence of two distinct metastable closed states that do not thermally equilibrate and are populated in a ratio that exclusively depends on the previous illumination color. Measuring action spectra following preillumination with either 410 nm or 690 nm light (Fig. 2*F*) revealed a pronounced shift in peak activity. Blue preillumination yielded a peak activity at 581 ± 1 nm, whereas red preillumination resulted in a peak activity at 543 ± 8 nm. Moreover, red preillumination not only shifted the action spectrum and reduced photocurrent amplitudes, but it also shifted the photon-dose–response curve to higher light intensities (*SI Appendix*, Fig. S3 *A* and *B*) and delayed channel *on*-kinetics (*SI Appendix*, Fig. S3*C*), while the *off*-kinetics remained unchanged. Preillumination-dependent spectral shifts were observed at pH 5 and 7.2 (*SI Appendix*, Fig. S3*D*) but were minimal at pH 9 (*SI Appendix*, Fig. S3*F*), where peak activity at 540 nm was unaffected by previous blue or red-light exposure. Comparison of light intensities required for channel opening, desensitization and resensitization with 660 nm or 405 nm light, respectively (*SI Appendix*, Fig. S4), showed that under 660 nm illumination, channel opening was more efficient than red-light desensitization (*SI Appendix*, Fig. S4 *A–C*), whereas under 405 nm light, lower intensities sufficed to restore red-light sensitivity than to open the channel (*SI Appendix*, Fig. S4 *D–F*).

Absorption measurements of detergent-solubilized recombinant CsChrimson confirmed the existence of two photochemically interconvertible protein states (Fig. 2*G*), which only partially recovered in the dark after red or UV illumination, but could be readily switched by the corresponding light colors (Fig. 2*H*). The overall spectral changes following red illumination were small but can be explained by accumulation of a blue shifted red light–adapted state (LA), which spectrally matches to the observed changes in photocurrent activity, with maximal increases and decreases at 480 nm and 595 nm, respectively (Fig. 2*I*).

FTIR Spectroscopy on the Formation of the Open State and the Red Light–Adapted State LA. To gain deeper insight into the molecular transitions underlying the D580 photocycle and its red-light adaptation, we performed cryotrapped Fourier transformed infrared (FTIR) spectroscopic measurements at pH 5. Stepwise cooling of Chrimson WT to 80 K effectively accumulated different photo stationary states during orange-light illumination (Fig. 3*A*) similar to the intermediates identified in our flash photolysis measurements (compare with Fig. 1*D*). Dark state bleaching was observed over the entire temperature range (GSB, blue), whereas the early photocycle intermediate P510 and the open-state P490 accumulated at 180 K and 240 K, respectively.

Since UV/Vis and action spectra shown in Fig. 2 *F*, *G*, and *I* demonstrate the existence of multiple stable photointermediates depending on pH and illumination conditions, we used similar protocols to record conformational changes and protonation changes by FTIR difference spectroscopy for transitions from i) the dark to the open state and ii) dark to the red light–adapted state for wild-type and the counterion mutant E165A (Fig. 3 *B–E*) at 240 K.

The difference spectra recorded after green illumination (523 nm) of the dark state represent the transition from D580 to the open-state P490 (Fig. 3 *B*, *Upper* line). The negative band at 1,655 cm^{-1} indicates small secondary structural changes, whereas the positive band at 1,178 cm^{-1} visualizes light-induced all-*trans*,15-*anti* to 13-*cis*,15-*anti* isomerization of the chromophore (26, 27). Moderate red-light exposure (633 nm, <30 s) yielded a similar spectrum (Fig. 3 *B*, *Central* line) likewise associated with P490 formation. However, subtle differences in the amide I region indicate the formation of the red light–adapted photoproduct (LA), albeit with a minor contribution. The lower spectrum in Fig. 3*B*, obtained after longer illumination with red light (>30 s), represents the further progressed transition from the dark state D580 to the red light–adapted state LA (as observed in our electrical and absorption measurements given in Fig. 2 *F* and *G*). The two bands at 1,640 (–) cm^{-1} and 1,184 (–) cm^{-1} particularly attracted our attention. The 1,640 (–) cm^{-1} band suggests that LA formation involves structural rearrangements different from those of the open state P490, and second, that perturbation of the retinal Schiff base could contribute to this transition (28, 29). The lack of the 1,178 (+) cm^{-1} band alongside with the appearance of the 1,184 (–) cm^{-1} band indicates an additional retinal isomerization reaction as a result of prolonged red illumination. A similar D_2O-sensitive negative band at 1,186 (–) cm^{-1} was previously observed in *Cr*ChR2 and assigned to the C14-C15 stretch vibration of the all-*trans*,15-*anti* retinal dark state, emerging due to retinal isomerization to 13-*cis*,15-*syn* *Cr*ChR2 (21). Accordingly, we suggest that also in Chrimson light adaptation likewise results from retinal double isomerization. We also expect that the retinal double isomerization occurs already early in the photocycle since the 1,184 (–) cm^{-1} band is already present in P680 stabilized at 80 K

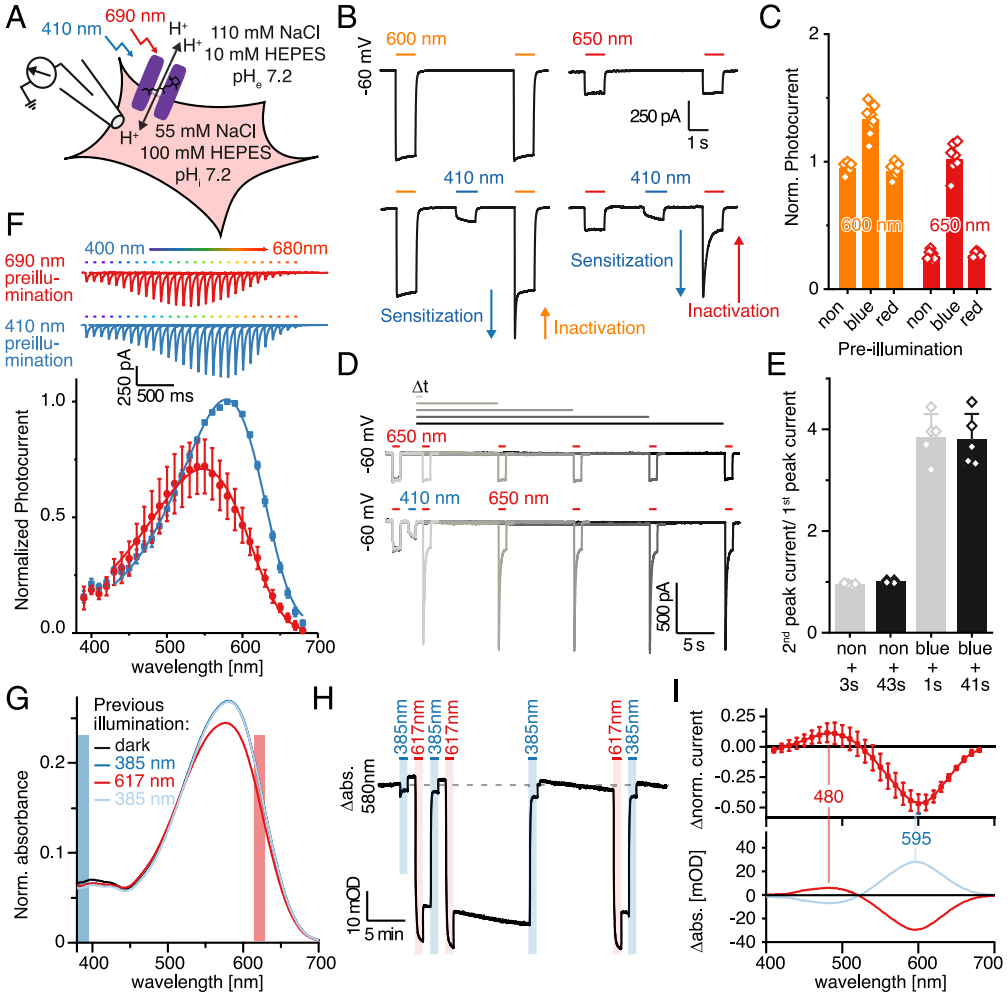

Fig. 2. Light adaptation of Chrimson. (*A*) Schematic of a HEK293 cell expressing CsChrimson (purple) with intracellularly pH clamped by 100 mM HEPES via the patch pipette, and photocurrents recorded in response to different colors of light. (*B*) Representative photocurrents at −60 mV during repetitive 1 s illumination with 600 nm or 650 nm light and without (*Top*) or with an additional intermediate UV pulse (*Bottom*)—measured as shown in *A*. (*C*) Normalized photocurrents evoked by 600 nm or 650 nm without (non) or following 1 s of 410 nm (blue) or 690 nm illumination (red) as shown in *B* (n = 5 to 8, normalized to the 1st light pulse at 600 nm). (*D*) Photocurrents at −60 mV during repetitive 650 nm illumination with dark intervals of increasing length, with and without an intermediate UV pulse. (*E*) Normalized peak photocurrent changes with or without intermediate UV illumination following short (1 or 3 s) or long (41 or 43 s) dark periods (n = 4 to 5, normalized as in *C*). (*F*) Preillumination-dependent action spectra: Cells were preilluminated at 0 mV for 2 s with either 410 nm (blue spectrum and traces) or 690 nm light (red spectrum and traces) before photocurrents in response to 10 ms illumination of different wavelengths but equal photon flux were recorded at −60 mV. *Top:* Representative traces of 690 nm preilluminated cells (red photocurrent traces on the top) or 410 nm preilluminated channels (blue photocurrent traces below). *Bottom:* Normalized peak amplitudes (n = 7 to 8). (*G*) UV–Vis spectrum of purified *Cs*Chrimson at pH 5 dark adapted (*black lines*) and following 60 s illumination with 385 nm (dark blue lines), 617 nm (*red line*), and again 385 nm light (light blue lines). Spectra are normalized to 280 nm absorption (not shown). (*H*) Absorption changes at 580 nm during alternating 385 nm and 617 nm illumination. (*I*) *Top:* Difference spectrum of normalized photocurrents following 690 nm and 410 nm preillumination as displayed in *F* (n = 7). *Bottom:* UV–Vis difference spectra (blue line: the initial 385 nm preilluminated spectrum minus the 617 nm preilluminated spectrum from *G*; red line: the same 617 nm preilluminated spectrum minus the 2nd blue preilluminated spectrum). Wavelengths of maximum absorption changes are indicated. All data are shown as mean ± SD.

(*SI Appendix*, Fig. S5), similar as previously discussed for CrChR2 (30).

Kinetic measurements at 240 K showed both, formation and decay of P490 (1,655 cm^{-1}, 1,178 cm^{-1}) upon 523 nm illumination as well as the transition into the LA state (1,640 cm^{-1}, 1,184 cm^{-1}) following prolonged exposure to 633 nm light. P490 formed instantaneously following green illumination (Fig. 3*C*, green lines), whereas the LA state accumulated within 300 s of red light (Fig. 3*C* red lines). After light off, P490 marker bands thermally decayed, whereas no decay of the LA to the dark-adapted state (D580) was observed on this time scale. Notably, alternating illumination with red and green light enabled reversible switching between the dark and LA state, as revealed by singular value decomposition (SVD) and rotational analysis (*SI Appendix*, Fig. S6).

Interestingly, the amide I bands (1,600 to 1,700 cm^{-1}) in the FTIR difference spectra of Chrimson, which indicate backbone rearrangements associated with channel opening, were small when compared to those of other ChRs, such as the C1C2 or ReaChR (Fig. 3*D*). In both of these opsins, the amide I bands increase in intensity from early photocycle to final formation of the conducting state, presumably due to helix hydration caused by an influx of water molecules into the ion-conducting pore as shown for CrChR2 (25, 31). In contrast, in Chrimson, the intensity remained small for the entire photocycle (80 to 260 K), suggesting that structural changes required for proton conduction occur early in the photocycle and involve markedly less helix hydration compared to other ChRs, thereby resembling the activation mechanism of proton pumps like bacteriorhodopsin (32, 33), Proteorhodopsin (3435, 36), or Archaerhodopsin-3 (37).

To compare the photoproducts of the dark and light-adapted state, we performed time-resolved measurements in which green laser flashes were applied to samples before or after red

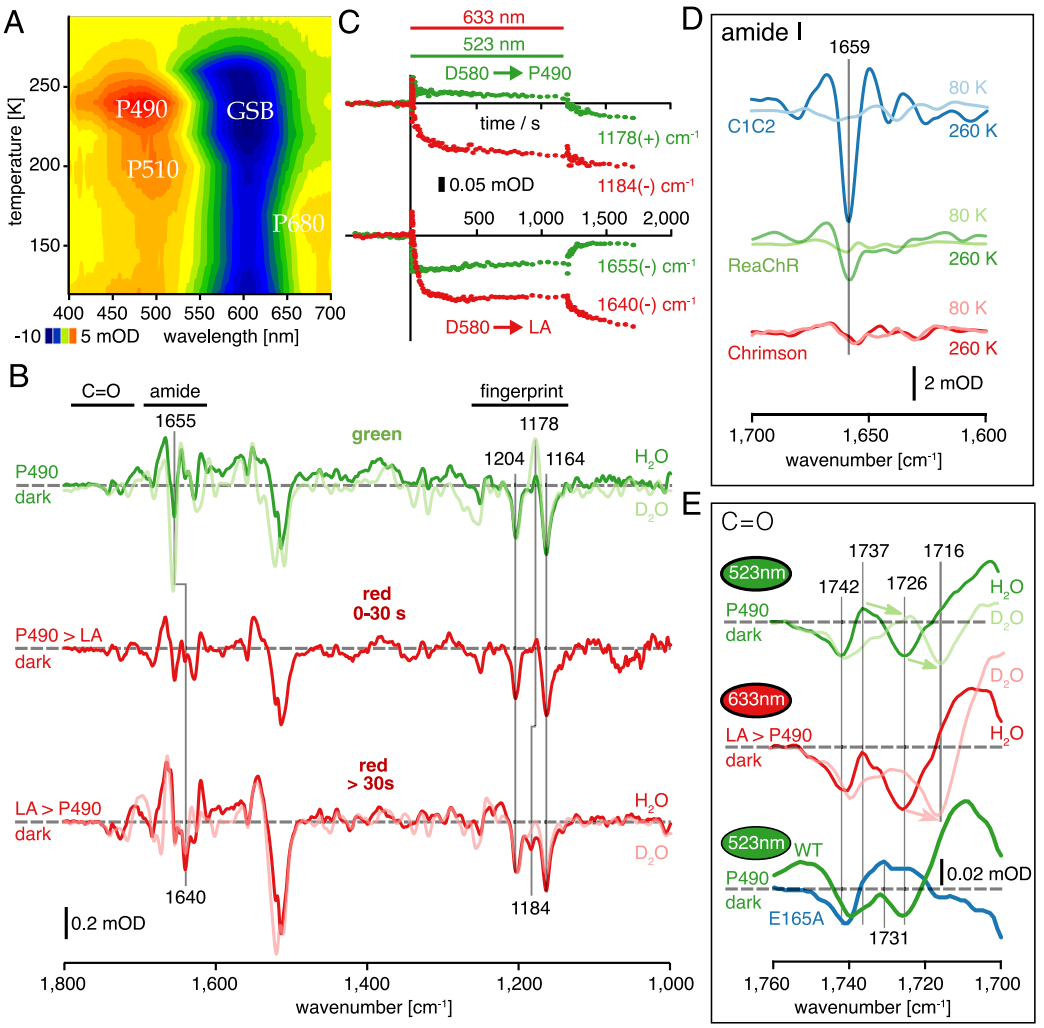

Fig. 3. Molecular changes during channel gating and light adaptation. (*A*) UV–Vis light–dark difference spectra of the CsChrimson wild-type at pH 5, recorded between 80 and 293 K during continuous illumination (λ_{max} ~ 594 nm), showing formation of P680, P510, and P490 and simultaneous ground state bleaching (GSB). (*B*) FTIR steady-state light–dark difference spectra of WT at pH 5 and 240 K. Green and short red illumination accumulate the conducting P490 state (*Upper* and *Central line*), while extended red illumination (>30 s) yields the red light–adapted state LA (*Lower line*). The D580→P490 and D580→LA photoreactions differ with respect to light-induced retinal isomerization and backbone changes. Measurements in D_2O are shown in light colors. (*C*) Kinetics of marker bands for P490 [green lines at 1,178 (+) cm^{-1} and 1,655 (−) cm^{-1}] and LA [red lines at 1,184 (−) cm^{-1} and 1,640 (−) cm^{-1}] after activation with green (λ_{max} ~ 523 nm) or red (λ_{max} ~ 633 nm) LEDs (colored bar) at 240 K, determined in two separate experiments. (*D*) FTIR light–dark difference spectra of C1C2 at pH 4, ReaChR at pH 5, and Chrimson at pH 5 induced by blue (λ_{max} ~ 471 nm), green (λ_{max} ~ 529 nm), and orange (λ_{max} ~ 594 nm) illumination, respectively. The backbone changes reflected by the band at 1,659 (−) cm^{-1} are most pronounced in C1C2 and least pronounced in Chrimson. While the large backbone changes occur in the transition to the assumed conducting state (260 K) in both C1C2 and ReaChR, the backbone changes in Chrimson largely occur already in the D580→P680 transition (80 K). (*E*) The υ(C = O) region of light/dark difference spectra of Chrimson wild-type in H_2O and D_2O at pH 5 and pD 5.0, respectively, and of the Chrimson mutant E165A mutant at pH 6.5. The arrows indicate bands shifting in D_2O.

preillumination (*SI Appendix*, Fig. S7). In the non-preilluminated sample, singular value decomposition (SVD) of the dataset identified only a single spectral component that was largely reminiscent of P490 formation with fast decay after light off (*SI Appendix*, Fig. S7*A*). Contrarily, in samples preilluminated for 60 s with red light, SVD revealed two spectral components (*SI Appendix*, Fig. S7*B*): one identical to P490, marked by all-*trans*,15-*anti* to 13-*cis*,15-*anti* isomerization [1,178 (+) cm^{-1}] and a second exhibiting the LA marker band for 13-*cis*,15-*syn* to all-*trans*,15-*anti* isomerization [1,184 (+) cm^{-1}], similar to that recorded during continuous red illumination (Fig. 3 *B*, *Lower* line) but inverted, as the LA state was preformed and then depleted by the green laser flash. We did not detect evidence for a new conducting state starting from LA, potentially a 13-*trans*,15-*syn* configuration, but instead, observed a transition back to the dark-adapted D580 state. Thus, the 13-*trans*,15-*syn*state either remains masked by the P490 signature, or alternatively, photoactivation of the LA state proceeds via C15=N isomerization that directly funnels into the conducting state P490 of the all-*trans*,15-*anti* photocycle—a plausible scenario given that the conducting state properties are highly similar whether initiated from D580 or from LA.

The Protonation State of the Counterion E165 During Channel Gating and Light Adaptation. To investigate protonation state changes and hydrogen bonding alterations during channel gating and light adaptation, we next analyzed the carbonyl region of the FTIR spectra (1,760 to 1,700 cm^{-1}) and compared spectra of green- and red-illuminated *Cs*Chrimson wild-type with those of the counterion mutant E165A (Fig. 3*E*). In the upper spectrum (wild-type), representing the transition from D580 (negative bands) to P490 (positive bands) upon continuous green illumination (dark green line), the band doublet at 1,737 (+) cm^{-1}/1,726 (–) cm^{-1} is downshifted in D_2O to 1,724 (+) cm^{-1}/1,716 (–) cm^{-1} (light green line). This pattern is attributed to E165 because it is absent

in the E165A mutant (lower spectrum, blue line). The shift of the band at 1,726 (–) cm^{-1} to 1,737 (+) cm^{-1} suggests a weakening of the hydrogen bond of E165 during P490 formation rather than its deprotonation (38). In the central spectrum, representing the transition from the dark state (D580) to the red light–adapted state (LA), a negative band at 1,728 cm^{-1} is observed in the wild-type (dark red line) that is shifted to 1,718 cm^{-1} in D_2O (light red line). The presence of a negative band with no positive counterpart indicates deprotonation of E165 in the LA state, in contrast to the hydrogen bond change of E165 upon green illumination. This assignment is further supported by the absence of this band in the E165A mutant spectrum (Fig. 3*E* lower spectrum, blue line).

Notably, the E165A spectrum was recorded at pH 6.5 due to sample instability at lower pH. At this pH, the wild-type spectrum (lower green line) also indicates E165 deprotonation upon green illumination, as evidenced by the single negative band at 1,728 cm^{-1}, identical to that observed in the LA state. A second negative band at 1,742 cm^{-1} in the wild-type spectra, which is only weakly sensitive to D_2O exchange and persists in the E165A mutant, may represent an additional, yet unassigned, deprotonation event. Furthermore, a positive band at 1,731 cm^{-1} appearing in the mutant spectrum, likely reflects protonation of another unidentified carboxyl group. In line with these spectral observations, photocurrents of the E165A mutant were reduced in amplitude and showed incomplete channel closure following red light adaptation. Interestingly, UV light reactivated the channel and promoted complete channel closure, indicating that similar dark and light adapted states exist in the mutant as in the WT (*SI Appendix*, Fig. S8 *A* and *B*). Accordingly, the spectral shift of peak activity between the dark- and light-adapted states was smaller but conserved (*SI Appendix*, Fig. S8*C*).

Light Adaptation of Chrimson Affects Neuronal Spike Fidelity and Red Light Excitation of Synaptic Transmission. To assess the functional impact of Chrimson's spectral shift for optogenetic applications in neurons, we expressed ChrimsonR (K176R) (4)—one of the most often applied Chrimson variants—in primary hippocampal cultures (Fig. 4*A*) and acute hippocampal slices (Fig. 4*I*) using adeno-associated viruses, and examined its ability to trigger APs and synaptic transmission under different illumination protocols.

Cultured hippocampal neurons expressing ChrimsonR-tdTomato were recorded in whole-cell current-clamp mode with the membrane potential set to –60 mV and postsynaptic currents blocked by 5 µM NBQX and 4 µM Gabazine. Neurons were stimulated with sets of ten 635 nm light pulses of increasing intensities (0.5 to 20 mW/mm^2) (Fig. 4 *B* and *C*). Before the first stimulation set (Baseline), cells were exposed to 405 nm light for 1 s to maximize Chrimson sensitivity. Subsequently, neurons were illuminated for 1 s with 635 nm light before repeating the 635 nm stimulation protocol. Finally, 1 s pulses of 405 or 470 nm light were applied prior to another round of red light stimulation. The preillumination wavelength significantly affected Chrimson function, reducing spike fidelity after red light inactivation but restoring activity after UV or blue light exposure (Fig. 4*C*). Following UV sensitization, the 50% spike success rate was reached at 3.3 mW/mm^2 of 635 nm light (95% CI: 2.8 to 3.7 mW/mm^2; Fig. 4*D*, black line), whereas inactivated Chrimson required 7.8 mW/mm^2 for half maximal spike success rates (95% CI: 6.9 to 8.9 mW/mm^2; red line). Preillumination with both UV or blue light fully restored Chrimson sensitivity to 635 nm light, yielding 50% spiking efficiency at 4.2 mW/mm^2 after 405 nm (Fig. 4*D*, purple line, 95% CI: 3.7 to 4.8 mW/mm^2) or 470 nm preillumination (Fig. 4*D*, blue lines, 95% CI: 3.7 to 4.6 mW/mm^2). Preillumination had no effect on spike fidelity at higher 635 nm intensities (20 mW/mm^2), indicating that at the given expression level, high light intensities invariably provide sufficient depolarization to induce AP firing. The most pronounced effect was observed at an intermediate 635 nm intensity (4 mW/mm^2), where inactivation by 635 nm light reduced spike success rates from 71 ± 13% to 10 ± 10%, while UV or blue light sensitization partially restored success rates to 53 ± 14 % and 46 ± 15 %, respectively (Fig. 4*E*). To further map Chrimson's light adaptation across the spectrum, preillumination at multiple wavelengths (385, 500, 525, 550, 580, 595, 660 nm) was tested (*SI Appendix*, Fig. S9 *A–J*). Preillumination at wavelengths ≤550 nm consistently enhanced spike success relative to the inactivated state, whereas wavelengths ≥580 nm reduced it (*SI Appendix*, Fig. S9*Q*). Even at lower intensities (1 mW/mm^2), blue light effectively reversed inactivation, while red light inactivation was less effective at lower power or shorter pulses (*SI Appendix*, Fig. S10 *A–D*). Nevertheless, only 2 to 3 repetitions of short 635 nm pulse trains were sufficient to significantly reduce spike success rates (Fig. 4 *F* (*Middle*), *G*, and *H*), whereas low intensity UV background illumination could prevent this effect (Fig. 4 *F* (*Bottom*), *G*, and *H*).

To determine whether light adaptation also occurs near Chrimson's activation peak, we repeated the same protocol using 595 nm light instead of 635 nm (*SI Appendix*, Fig. S11*A*). The adaptation effect was markedly reduced: at 3 mW/mm^2, only minor differences were observed between sensitized and inactivated states, and spike success rates converged at 4 mW/mm^2 (Baseline: 42.3 ± 13.4 %; Inactivation: 40 ± 13%; Sensitization: 41.5 ± 13.4%, *SI Appendix*, Fig. S11 *B–D*), indicating that 595 nm stimulation is largely insensitive to illumination history. Consistently, repetitive 595 nm stimulation maintained stable firing (Fig. 4 *F*, *Top*). This behavior aligns with the weaker red-light adaptation observed at 600 nm compared with 650 nm in HEK293 cells (Fig. 2*B*), likely because 595 nm light activates both the D580 and LA states of Chrimson.

To test whether the adaptation-induced spectral shifts also affect Chrimson's efficacy to drive transmitter release from axon terminals (4, 39, 40), ChrimsonR-EGFP was expressed in CA3 pyramidal neurons of GRIK-4 Cre mice using a Cre-dependent AAV (Fig. 4 *I*, *Top*). Optically evoked field excitatory postsynaptic potentials (fEPSPs) were recorded in the contralateral CA1 *stratum radiatum* (Fig. 4 *I*, *Bottom*). Repetitive 635 nm stimulation (5 ms, 635 nm, 3 mW/mm^2) was applied locally at commissural CA3-CA1 projections to evoke synaptic transmission, followed by 1 s pulses of 405 nm, 470 nm (sensitization), or 635 nm (inactivation) (Fig. 4 *J* and *K*). UV sensitization (405 nm, 10 mW/mm^2) rapidly increased fEPSP amplitudes to 189 ± 22% (Fig. 4*L*), which returned to baseline within 5 min (*SI Appendix*, Fig. S12 *A* and *B*). Conversely, prolonged 635 nm illumination reduced fEPSP amplitudes to 54 ± 14% (Fig. 4*H*), followed by gradual recovery. Notably, 470 nm had a weaker sensitizing effect than UV light (Fig. 4*L*, 128 ± 23%).

Together, these experiments demonstrate that also in neurons Chrimson's multiple dark states are bidirectionally interconverted by distinct wavelengths, particularly 635 nm and 405 nm light, and significantly modulate red light–driven performance at both the somatodendritic and axonal levels.

Discussion

In the present manuscript, we elucidate light adaptation and the resulting photocurrent modulation of the red light–activated ChR Chrimson. The complexity of Chrimson arises from the interplay of at least three distinct closed states that coexist in the dark in varying proportions depending on pH and illumination history (Fig. 5). Remarkably, all three closed states differ in their

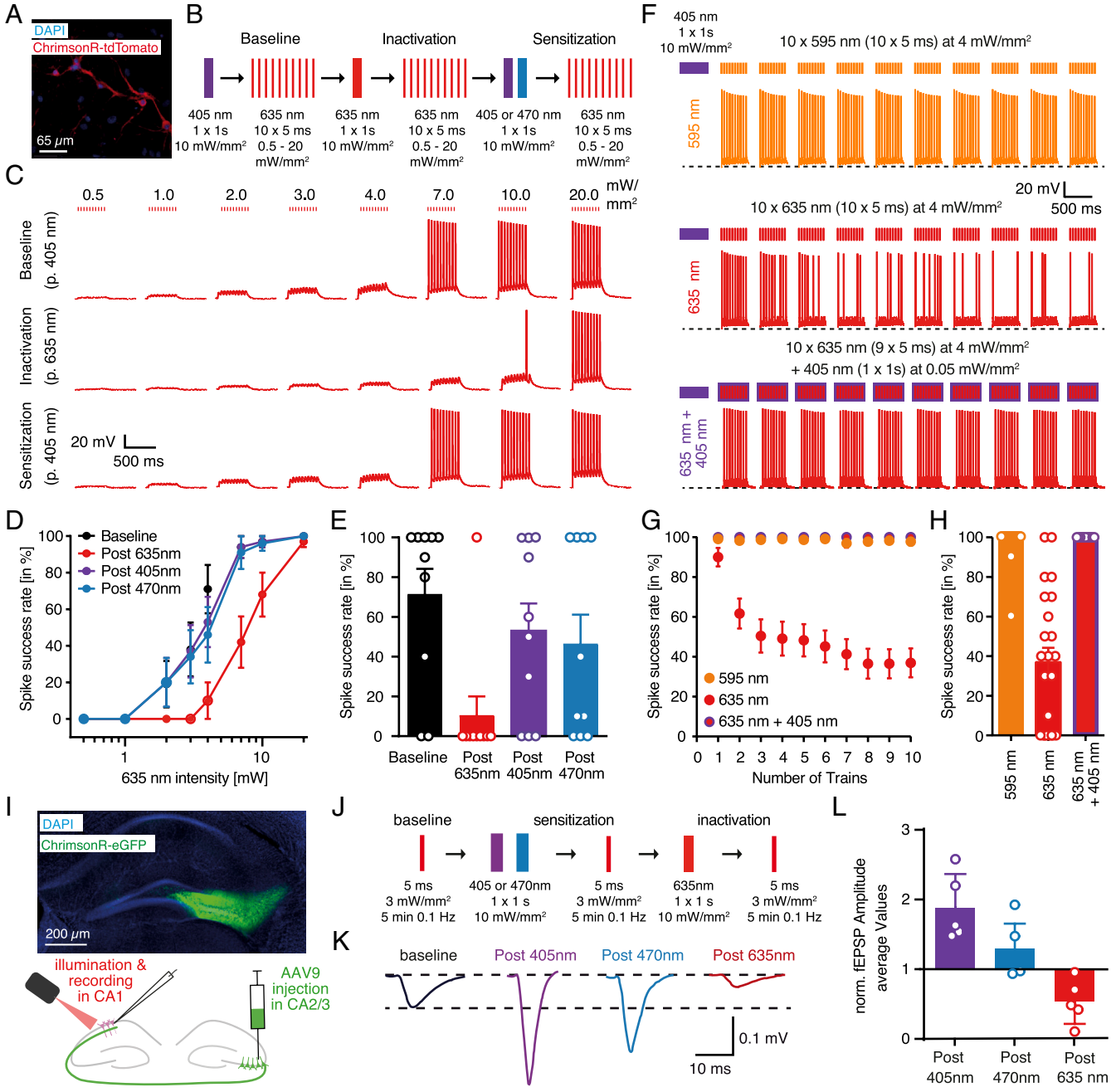

Fig. 4. Physiological consequences of the light adaptation and spectral shift of Chrimson in neurons. (*A*) Fluorescent image of hippocampal neurons transduced with AAV2/9 encoding ChrimsonR-tdTomato. (*B*) Photostimulation protocol: APs were evoked using eight trains of 10 pulses (5 ms, 635 nm, 20 Hz) of increasing light intensities. Before each series of 635 nm flashes, neurons were preilluminated with 405 nm or 635 nm light (1 s at 10 mW/mm^2). (*C*) Example traces of 635 nm light-evoked spiking. *Upper* panel: baseline condition following 405 nm preillumination. *Middle* panel: reduced spike fidelity after 635 nm preillumination. *Lower* panel: recovery of AP firing after 405 nm preillumination. (*D*) Spike probability after 635 nm preillumination (red) compared to non-preilluminated cells (baseline, black), and those preilluminated with 405 nm (purple) and 470 nm (blue) to restore AP firing probability. 50% AP success rate was at baseline (black): 2.8 to 3.7 mW/mm^2; post 635 nm (red): 6.9 to 8.9 mW/mm^2; post 405 nm (purple): 3.1 to 4.2 mW/mm^2; post 470 nm (blue): 3.2 to 4.5mW/mm^2, all stated as 95% CI, n = 10). (*E*) Comparison of preillumination effects on AP fidelity at 4 mW/mm^2 635 nm flashes, showing recovery of spiking across conditions (baseline: 71 ± 13%; post 635 nm: 10 ± 10%; post 405 nm: 53 ± 14%; and post 470 nm: 46 ± 15%, n = 10). (*F*) Repetitive stimulation of hippocampal neurons with bursts of light flashes at 595 nm (*Upper*), 635 nm (*Middle*), or 635 nm combined with 1 s of 405 nm and background illumination (*Lower*). (*G*) Spike success rate across stimulation trains for each protocol. Repeated 635 nm stimulation led to a progressive loss of sensitivity, which was prevented by the addition of 405 nm light. Spike success remained stable with 595 nm stimulation (n = 23). (*H*) Spike success rate after 10 trains as shown in *F* (595 nm, 97.8 ± 8.5%; 635 nm, 36.9 ± 34.7%; 635 + 405 nm, 100 ± 0.0%; n = 11 to 23). (*I*) Fluorescent image of the hippocampal formation showing ChrimsonR-eGFP expression in CA3 pyramidal neurons, achieved via unilateral AAV2/9 injection into CA3. Field excitatory postsynaptic potentials (fEPSPs) were recorded from contralateral CA1 in acute coronal hippocampal slices. (*J*) fEPSPs were optogenetically evoked using 5 ms pulses of 635 nm light (3 mW/mm^2). Sensitization was induced with 405 nm or 470 nm light and reversed with 635 nm preillumination (1 s, 10 mW/mm^2). (*K*) Example fEPSP traces under different preillumination conditions: baseline (black), 405 nm (purple), 470 nm (blue), and 635 nm (red). (*L*) Quantification of normalized fEPSP amplitudes following spectral shift experiments, illustrating wavelength-dependent modulation of synaptic strength (405 nm: 189 ± 22%, 470 nm: 128 ± 23%, 635 nm: 54 ± 14% of baseline; n = 5, N = 3). All data are shown as mean ± SEM.

absorption color and, upon activation, give rise to distinct open states with important consequences for Chrimson's photocurrent properties and optogenetic application.

The most red-shifted closed state of Chrimson is the acidic dark state D580, which coexists with the alkaline D520 at a neutral pH. Both states differ in the protonation of the counterion E165

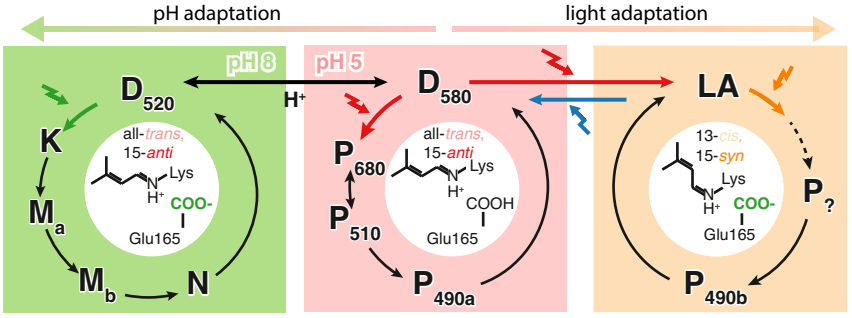

Fig. 5. Dark state heterogeneity and alternative photocycles of Chrimson. Photo transitions of Chrimson can be described by three distinct photocycles, whose populations depend on pH and preceding illumination color. At acidic and neutral pH, the red light–absorbing dark state D580 harbors an all-*trans*,15-*anti* retinal, and a protonated counterion, Glu165. Upon red light exposure, all-*trans* → 13-*cis* isomerization triggers channel opening, leading to the highly conductive, proton-selective P490 state, characterized by hydrogen bond rearrangements of Glu165. Concurrently, double isomerization (all-*trans*,15-*anti* → 13-*cis*,15-*syn*) leads to formation of the light-adapted closed state LA, featuring a deprotonated Glu165 and blue shifted peak absorption. LA remains photoactive, either reverting to D580 or entering its own photocycle, which, through an as-yet-unknown sequence of intermediates, gives rise to a P490-like open state (P490b). At alkaline pH, Glu165 undergoes deprotonation, shifting the dark state equilibrium toward the green light-absorbing D520, that upon green light absorption follows a bacteriorhodopsin-like photocycle featuring a late M-state and an N-state, both of which correspond to a low-conductance yet cation-permeable open state.

(17, 18), which not only determines their absorption color but also leads to two distinct photocycles upon light activation. The D520 photocycle closely resembles those of other chlorophyte ChRs (21, 41, 42). Channel opening is preceded by an outward-directed charge transfer (43), and coincides with a late, long-lived M-state with a deprotonated chromophore, and the following N-state, similar as in *Cr*ChR2 (21). The charge transfer and extended M-state lifetime resemble those of *Ca*ChR1 from *Chlamydomonas augustae* (43), which shares a similar counterion configuration with Chrimson, including a phenylalanine in helix 2 that modulates the counterion pK_a (44). In contrast, the D580 photocycle differs from all other known ChRs. It features a blue-shifted open-state P490 formed without detectable deprotonation of the retinal Schiff base. Instead, P490 forms through a sequence of blue-shifted photocycle intermediates, exhibiting spectral diffusion en route to the open state (19). Channel opening in P490 involves only minor structural rearrangements, comparable to those in rhodopsin proton pumps (3432, 33, 36, 37). It is facilitated by reorganization of the hydrogen bonding network within the counterion complex, leading to E165 deprotonation at more alkaline conditions (Fig. 3*E*), and involves an additional, yet-unidentified side chain deprotonation—possibly E139 or E300, given their proximity to the active site (18) and their strong influence on photocurrent kinetics (16). These subtle rearrangements are sufficient for channel opening, as H^+ conductance in Chrimson does not require the formation of a fully hydrated pore, as observed in *Cr*ChR2 (25), but may proceed via proton hopping along a chain of water molecules and carboxylate residues in a Grotthuss-like mechanism, as proposed for other H^+ channels (45).

Although both photocycles shape Chrimson's photocurrents, photoproducts of D580 dominate even at pH 8, as evidenced by the action spectra and single-turnover kinetics. This dominance may result from a higher counterion pK_a in cells compared to the isolated protein, as not only voltage, but also lipid interaction had been shown to affect Chrimson's D520/D580 equilibrium (17). Alternatively, it could reflect differences in the quantum yield of both dark states, which is lower in Chrimson [~20%, (19)] than in other ChRs [~30%, (42)] and proton transporters [~67% for bacteriorhodopsin, (46)] or a higher single-channel conductance of the P490 open state compared with those of the D520 photocycle. The existence of distinct open states in both photocycles may further explain conflicting reports on Chrimson's ion selectivity, with some studies suggesting conventional *Cr*ChR2-like selectivity at pH 9 (14) whereas others report high proton selectivity at neutral and acidic pH (16).

Most importantly, continuous red illumination induces the accumulation of a third, blue-shifted, red-light-adapted closed state, termed LA. Formation of the LA state is driven by an additional C15=N *anti–syn* isomerization of the retinylidene chromophore, which occurs with a certain probability in conjunction with the obligatory 13-*trans*-to-*cis* isomerization. This generates *13-cis,15-syn* retinal—an inactive configuration also observed in other ChRs during prolonged illumination (30, 47). In Chrimson, however, this double isomerization results in a pronounced blue shift - an effect not seen in other ChRs (8, 21), but reminiscent of the hypsochromic shift observed between the same retinal isomers in bacteriorhodopsin (absorbing at 548 and 568 nm respectively), which shares a conserved retinal-binding pocket with Chrimson. Yet, whereas in bacteriorhodopsin both isomers equilibrate in the dark (48), in Chrimson, the *13-cis,15-syn* configuration accumulates only after red-light illumination. We further assume that in Chrimson, excitation of either closed states—D580 (*all-trans,15-anti*) or LA (*13-cis,15-syn*)—can lead to channel opening, whereas in bacteriorhodopsin only the *all-trans,15-anti* form promotes proton pumping (49). Chrimson's activation kinetics differ depending on which preillumination-dependent dark state is excited, but the closing kinetics and ion selectivity remain unchanged, suggesting that the conducting states of the *syn*- and *anti*-cycles are similar or nearly identical. Considering the lack of information about the syn-cycle open-state P490b (Fig. 5), it is conceivable that photoactivation of the LA state directly triggers C15=N syn to anti isomerization, yielding the same chromophore configuration as previously discussed for P490a, thereby explaining the rapid photochemical return of the LA state to the D580 conformation. In LA, the counterion E165 deprotonates, which however cannot solely account for the blue shifted LA spectrum, as a smaller light-induced blue shift persists in the E165A mutant, likely reflecting differences in retinal isomer absorption. Notably, in this mutant the LA state also becomes leaky, underscoring that only subtle structural changes control whether Chrimson is open or closed.

Similar photochromic shifts between dark- and light-adapted states have also been reported for other opsins—most prominently Anabaena sensory rhodopsin, which undergoes a transition from *all-trans,15-anti* to *13-cis,15-syn* retinal upon photoexcitation (50)—and more recently for rhodopsin-based voltage sensors of the QuasAr family, such as NovArch (51), which shows enhanced

red fluorescence under simultaneous blue illumination, and in red-light-sensitive anion channels such as RubyACRs (52), which strongly desensitize under red light but can be partially reactivated by blue-light pulses (53). The molecular mechanisms underlying these effects are diverse and often remain poorly understood. In QuasArs, voltage and light modulate transitions between protonated and deprotonated chromophores with mixed isomer composition (54). In RubyACRs, absorption of a second photon by an early but long-lived red-shifted photointermediate populates two additional long-lived, yet still photoactive, blue- and UV-sensitive light-adapted states. A similar early photocycle branching is also conceivable for Chrimson, as light-adapted marker bands have already been observed at 80 K. However, whereas RubyACRs nearly completely inactivate during continuous illumination, in Chrimson, the presence of similar conductive states in both photocycle branches—D580 and LA, respectively—as well as substantial spectral overlap of both dark states, favors rapid equilibration between them and provides a spectral range near Chrimson's activation maximum that ensures stable and sustained channel activity.

Finally, the multicolor photoresponses of Chrimson have significant implications for its optogenetic applications. Despite the discovery of over a thousand ChRs in recent years (55, 56), Chrimson continues to be the most red-shifted excitatory ChR, even a decade after its initial characterization (4). Therefore, it is the opsin of choice for many multicolor applications in various host systems (1) and is frequently used in combination with blue light–sensitive opsins or enzymes, either expressed in different cell populations (4), coexpressed within the same cell (57), or fused within the same protein framework (10). To minimize optical crosstalk, Chrimson is frequently activated at wavelengths far beyond its activation maximum. For ChRmine, this approach has enabled transcranial neuronal activation (58), but for Chrimson, the red-shifted activation causes successive reductions in photocurrent amplitudes as the protein shifts to the LA state. This phenomenon of light adaptation can be mitigated by stimulating Chrimson at its activation maximum—580 nm for Chrimson WT or ChrimsonR and 610 nm for the most red-shifted variant, ChrimsonSA—and can be reversed by short pulses of weak UV light or blue background illumination. Red light desensitization and blue light potentiation of Chrimson photoresponses have previously been observed when combining Chrimson with the blue light–activated cyclase bPAC (57) or other blue light–sensitive ChRs (59), but a molecular explanation could not be provided so far.

In conclusion, we elucidate the complex interplay of simultaneous photocycles in Chrimson, demonstrating that red light activation is influenced not only by absorption properties but also by the performance and conductance of distinct photocycle states. Our findings highlight the significance of light adaptation in shaping Chrimson's photocurrents and underscore the need to consider illumination history when designing optogenetic experiments or therapeutic interventions. Moreover, these insights provide a foundation for developing multicolor illumination protocols, where sequential or combined blue and red illumination could enhance Chrimson's functionality and stability in both basic neuroscience research and medical applications.

Materials and Methods

DNA Preparation and Molecular Biology. For yeast expression, humanized cDNA of CsChrimson (GenBank™: KJ995863.2, 1-345 AA) was inserted in-frame with the N-terminal yeast consensus sequence [AATAATGTCT, (60)] and a C-terminal TEV protease cleavage site (ENLYFQG) and cloned into pPICZ-C (Thermo Fisher Scientific, USA) between EcoRI/SalI (Thermo Fisher, USA). For expression in HEK293 and ND7/23 cells, CsChrimson was cloned into the pmCerulean-C1 vector as previously described (16). For neuronal expression, pAAV-Syn-FLEX-rc [ChrimsonR-GFP] (Addgene plasmid #84480) and pAAV-Syn-ChrimsonR-tdTomato [Addgene plasmid #59171(4)] were kindly provided by Edward Boyden and packed into AAV9 viruses by the Viral Core Facility (VCF) of Charité Berlin. Site-directed mutagenesis was performed using a QuickChange Site-Directed Mutagenesis Kit (Agilent Technologies, Santa Clara, CA), according to the manufacturer's instructions.

Chrimson Expression in Mammalian Cell Cultures. Electrophysiological recordings were performed on transiently transfected HEK293 and ND7/23 cells, prepared as previously described (61). Briefly, cells were cultured at 5% CO_2 and 37 °C in Dulbecco's minimal essential medium supplemented with 1 μM all-*trans*-retinal, 100 μg/mL penicillin/streptomycin, and either 10% fetal bovine serum (FBS) for HEK cells or 5% FBS for ND7/23 cells (Biochrom, Berlin, Germany). For patch-clamp recordings, cells were seeded on polylysin-coated coverslips at a concentration of 0.4 to 0.75 × 10^5 cells/mL and transiently transfected using the FuGENE® HD Reagent (Promega, Madison, WI) 28 to 48 h before measurement.

Patch-Clamp Experiments in HEK293 and ND 7/23 Cells. Whole-cell patch-clamp recordings were conducted on two independent experimental setups equipped with five separate light sources for pulsed and continuous illumination, combining previously described procedures (16, 21, 62) described in greater detail in *SI Appendix, Extended Methods*.

Expression and Purification in *P. pastoris*. Transformation and expression in the methylotrophic yeast *P. pastoris* were done as described before (6364, 65). CsChrimson proteins were purified by affinity chromatography (His-Trap Crude FF, 5 mL) and desalting (HiPrep-26/10). pH was adjusted to pH 6.5 during the desalting step. Similar also C1C2 and ReaChR samples were prepared as previously described (8, 30, 42) and stored in 20 mM citrate containing 100 mM NaCl and either 0.05% (w/v) n-dodecyl β-D-maltoside (DDM) adjusted to pH 4 for C1C2 or 0.03 % (w/v) DDM adjusted to pH 5 for ReaChR, respectively.

Ultraviolet-Visible Absorption Spectroscopy. Absorption spectra were recorded with a Cary 50 spectrophotometer (Varian Inc., Palo Alto, CA) at 22 °C. Light for dual-color experiments was provided by a multi-LED module (BioLED, Mightex Systems, Toronto, ON, Canada) equipped with a red (617 nm, 2.48 × 10^{16} photons mm^{-2} s^{-1}) and a UV LED (385 nm, 2.57 × 10^{16} photons mm^{-2} s^{-1}). Transient UV–Vis spectroscopy was performed according to Krause and Kaufmann et al. (8, 41) with a more detailed description provided in *SI Appendix, Extended Methods*.

FTIR Measurements. FTIR samples in citrate buffer (20 mM citrate, 100 mM NaCl, pH 5), HEPES buffer (20 mM HEPES, 100 mM NaCl, pH 6.5), and 0.03 % (w/v) DDM were prepared on a BaF_2 window by repeated drying under a nitrogen stream and subsequent rehydration and sealed with a second BaF_2 window. Samples were illuminated with LEDs (maximum emission wavelength ~400 nm for UV, ~530 nm for green, and ~610 nm for red illumination). For cryostatic measurements, the cryostat DN (Oxford Instruments, Abingdon, UK) was used. Samples were equilibrated at the respective temperature for at least 45 min. After measurement, the sample was heated up again to a minimum of 20 °C to allow relaxation.

Cryostatic FTIR measurements were performed using an ifs66v/s FTIR spectrometer (Bruker Optics, Karlsruhe, Germany) with an LN_2-cooled mercury cadmium telluride detector (Kolmar Technologies, Newburyport, MA). An 1,850 cm^{-1} optical cut-off filter was used. Spectra were recorded with a 200 kHz sampling rate and a spectral resolution of 2 cm^{-1}. The difference spectra were corrected for baseline drifts using a spline algorithm and the baseline-correction mode implemented in the OPUS 6.5 software package (Bruker Optics, Karlsruhe, Germany).

Laser-induced FTIR measurements were performed with a Vertex 80v FTIR Spectrometer (Bruker Optics, Karlsruhe Germany) equipped with a liquid N_2-cooled MCT detector (Kolmar Technologies, Newburyport, MA). An 1,850 cm^{-1} optical cut-off filter was used. Spectra were recorded with a 300 kHz sampling rate and a spectral resolution of 4 cm^{-1}. After an equilibration time of at least 60 min, red preillumination was performed with a set of LEDs over 60 s. The single turnover excitation was achieved with a 10 Hz pulsed Nd:YAG Powerlite 9010 LASER as a pump source for a Horizon II optical parametric oscillator (Continuum, San Jose, CA) set to green light. The pulse width of the setup was in the range of 3 to

7 ns, and the energy output was approximately 120 mJ. The recorded difference spectra were preprocessed and baseline-corrected with the OPUS 7.5 software package (Bruker Optics, Karlsruhe, Germany). The FTIR data were analyzed as described before (66, 67). Assuming a sequential reaction scheme, a sum of exponential functions was used as a fit model.

Animal Experiments. All animal experiments complied with Directive 2010/63/EU on the protection of animals used for scientific purposes and were approved by local authorities in Berlin (LAGeSo, license number G0030/20). Mice were bred at the Charité animal facility and housed in individually ventilated cages (3 to 4 per cage) under a 12-h light–dark cycle, with ad libitum access to food and water.

Neuronal Cell Culture. Newborn C57BL/6 N mice of either sex were decapitated, and their brains were rapidly transferred to an ice-cooled Petri dish. Hippocampal cells were enzymatically dissociated using Papain, followed by manual trituration. Neurons were plated onto glial feeder cells at a density of 3.5×10^4 cells per well in 24-well plates containing coverslips coated with collagen and poly-D-lysine. Cells were cultured in Neurobasal-A medium supplemented with 2% B27 and 0.2% penicillin/streptomycin (all Invitrogen) at 37 °C, 5% CO_2. AAV9 encoding Syn-ChrimsonR-tdTomato was added 1 to 4 d postplating. Cells were used for electrophysiological recordings after 14 to 21 d in vitro.

Electrophysiology in Primary Neurons. Whole-cell current-clamp recordings were performed on an IX73 inverted microscope (Olympus, Shinjuku, Tokyo, Japan) using a Multiclamp 700B amplifier under the control of a Digidata 1550 AD board and Clampex 10 software (all Molecular Devices). Recordings were performed at room temperature. Data were acquired at 10 kHz and filtered at 3 kHz. A TTL-controlled-LED system (pE4000, CoolLED, Andover, UK) was coupled into the backport of the IX73 microscope by a single liquid light guide. Fluorescent light was passed through a quad-band filter set (AHF, Tübingen, Germany, cat. no. F66-415) and an Olympus UPLSAPO 20×, NA 0.75 objective. The extracellular solution contained (in mM): 140 NaCl, 2.4 KCl, 10 HEPES, 10 glucose, 2 $CaCl_2$, 4 $MgCl_2$ (pH adjusted to 7.3 with NaOH, 300 mOsm). The intracellular solution contained (in mM): 135 KCH_3SO_3, 4 NaCl, 2 $MgCl_2$, 10 HEPES, 2 Na_2ATP, 0.3 NaGTP, 0.06 EGTA, 0.01 $CaCl_2$, pH adjusted to 7.2 with KOH, 300 mOsm. All chemicals were purchased from Tocris, Merck, or Carl Roth. In whole-cell current-clamp recordings, membrane potential was manually set to −60 mV. Postsynaptic currents were suppressed by an application of 5 µM NBQX (2,3-dioxo-6-nitro-7-sulfamoyl-benzo[f]quinoxaline) and 4 µM SR-95531 (Gabazine). At the beginning and the end of each recording, the AP fidelity was checked with a train of 10× 5 ms 550 nm flashes at 20 Hz with increasing intensities (0.5, 1, 2, 3, 4, 7, 10, 20 mW mm^{-2}). Neurons with decreasing firing fidelity were excluded from the analysis. APs were analyzed with AxoGraph X (Sydney, Australia).

Stereotactic Viral Injection in Grik4-Cre Mice and Electrophysiology on Hippocampal Slices. Female Grik4-Cre mice (68) were anesthetized with 1.5% isoflurane (vol/vol in oxygen) and monitored at a constant body temperature of 37 °C. AAVs (serotype 9) were stereotaxically injected into the right dorsal CA3 region following previously established protocols (69). All animals recovered fully within days and were maintained for three weeks before slice preparation and electrophysiological recordings. These were performed similar to previous studies (69), and a comprehensive description of the procedures can be found in *SI Appendix, Extended Methods*.

Data Analysis and Statistics. Electrical recordings were analyzed using the Clampfit 10.7 software (Molecular Devices), Microsoft Excel, Origin 2018® (OriginLab, Northampton, MA) and GraphPad Prism 9.5.1 (GraphPad Software, Boston, MA). Photocurrent traces were baseline corrected, filtered, and reduced in size for display purposes. For single turnover laser measurements, each acquired sweep was time-shifted postmeasurement to align it with the rising edges of the Q-switch signals of the activating laser pulses and binned to 50 logarithmically spaced data points per temporal decade with a custom-written MATLAB script as described before (MathWorks, Natick, MA) (21). The exact number of biological replicates for each measurement is provided in the figure legend, with n stating the number of cells recorded in cultures or the number of slices in fEPSP recordings.

Data, Materials, and Software Availability. All study data are included in the article and/or *SI Appendix*.

ACKNOWLEDGMENTS. We thank Maila Reh, Sandra Augustin, and Monika Dopatka for excellent technical assistance, Tobias Rose and Christiane Grimm for helpful discussions, and the Viral Core Facility of the Charité Berlin for adeno-associated viruses. The work was supported by the German Research Foundation: EXC-2049-390688087, P.H., J.V., L.T., and D.S.); SFB 1078 No. 221545957, F.B., SFB1315 No. 327654276, P.H., J.V., B.R.R., and D.S., SPP1926 No. 425994138, P.H. and B.R.R., the European Research Council Horizon 2020 program (BrainPlay Grant Agreement No. 810580, D.S.), and the EINSTEIN Foundation Berlin (Grant ID EZ-1014-226, D.S.). P.H. is a Hertie Professor for Biophysics and Neuroscience and is supported by the Hertie Foundation.

Author affiliations: [a]Charité–Universitätsmedizin Berlin, Corporate Member of Freie Universität Berlin and Humboldt-Universität zu Berlin, Neurosciences Research Center, Berlin 10117, Germany; [b]Institute of Biology, Experimental Biophysics, Humboldt-Universität zu Berlin, Berlin 10115, Germany; [c]Institute of Biology, Biophysical Chemistry, Humboldt-Universität zu Berlin, Berlin 10115, Germany; and [d]German Center for Neurodegenerative Diseases, Berlin 10117, Germany

Author contributions: J.V., F.B., and P.H. designed research; J.V., J.C.D.K., L.F., L.T., B.S.K., P.F., T.B.T.N., and B.R.R. performed research; D.S. and P.H. contributed new reagents/analytic tools; J.V., J.C.D.K., L.F., P.F., B.R.R., F.B., and P.H. analyzed data; and J.V., J.C.D.K., B.R.R., F.B., and P.H. wrote the paper.

Reviewers: L.S.B., University of Guelph; A.E.C., Harvard University; E.G.G., The University of Texas Health Science Center at Houston Department of Biochemistry and Molecular Biology; and B.R., Institute of Molecular and Clinical Ophthalmology Basel.

The authors declare no competing interest.

1. V. Emiliani *et al.*, Optogenetics for light control of biological systems. *Nat. Rev. Methods Primers* **2**, 55 (2022).
2. E. S. Boyden, F. Zhang, E. Bamberg, G. Nagel, K. Deisseroth, Millisecond-timescale, genetically targeted optical control of neural activity. *Nat. Neurosci.* **8**, 1263–1268 (2005).
3. R. Weissleder, A clearer vision for in vivo imaging. *Nat. Biotechnol.* **19**, 316–317 (2001).
4. N. C. Klapoetke *et al.*, Independent optical excitation of distinct neural populations. *Nat. Methods* **11**, 338–346 (2014).
5. O. Yizhar *et al.*, Neocortical excitation/inhibition balance in information processing and social dysfunction. *Nature* **477**, 171–178 (2011).
6. J. H. Marshel *et al.*, Cortical layer-specific critical dynamics triggering perception. *Science* **365**, eaaw5202 (2019).
7. J. Y. Lin, P. M. Knutsen, A. Muller, D. Kleinfeld, R. Y. Tsien, ReaChR: A red-shifted variant of channelrhodopsin enables deep transcranial optogenetic excitation. *Nat. Neurosci.* **16**, 1499–1508 (2013).
8. B. S. Krause *et al.*, Complex photochemistry within the green-absorbing Channelrhodopsin ReaChR. *Biophys. J.* **112**, 1166–1175 (2017).
9. A. M. Stamatakis *et al.*, Simultaneous optogenetics and cellular resolution calcium imaging during active behavior using a miniaturized microscope. *Front. Neurosci.* **12**, 1–16 (2018).
10. J. Vierock *et al.*, BiPOLES is an optogenetic tool developed for bidirectional dual-color control of neurons. *Nat. Commun.* **12**, 4527 (2021).
11. J. Wietek *et al.*, A bistable inhibitory optoGPCR for multiplexed optogenetic control of neural circuits. *Nat. Methods* **21**, 1275–1287 (2024).
12. M. H. W. Yap *et al.*, Oscillatory brain activity in spontaneous and induced sleep stages in flies. *Nat. Commun.* **8**, 1815 (2017).
13. J. H. Simpson, L. L. Looger, Functional imaging and optogenetics in *Drosophila*. *Genetics.* **208**, 1291–1309 (2018).
14. T. Mager *et al.*, High frequency neural spiking and auditory signaling by ultrafast red-shifted optogenetics. *Nat. Commun.* **9**, 1750 (2018).
15. J. A. Sahel *et al.*, Partial recovery of visual function in a blind patient after optogenetic therapy. *Nat. Med.* **27**, 1223–1229 (2021).
16. J. Vierock, C. Grimm, N. Nitzan, P. Hegemann, Molecular determinants of proton selectivity and gating in the red-light activated channelrhodopsin Chrimson. *Sci. Rep.* **7**, 1–15 (2017).
17. D. Urmann *et al.*, Photochemical properties of the red-shifted Channelrhodopsin Chrimson. *Photochem. Photobiol.* **93**, 782–795 (2017).
18. K. Oda *et al.*, Crystal structure of the red light-activated channelrhodopsin Chrimson. *Nat. Commun.* **9**, 3949 (2018).
19. I. H. M. Van Stokkum *et al.*, Reaction dynamics in the Chrimson Channelrhodopsin: Observation of product-state evolution and slow diffusive protein motions. *J. Phys. Chem. Lett.* **14**, 1485–1493 (2023).
20. M. Saita *et al.*, Photoexcitation of the P_4^{480} state induces a secondary photocycle that potentially desensitizes Channelrhodopsin-2. *J. Am. Chem. Soc.* **140**, jacs.8b03931 (2018).
21. J. Kuhne *et al.*, Unifying photocycle model for light adaptation and temporal evolution of cation conductance in channelrhodopsin-2. *Proc. Natl. Acad. Sci. U.S.A.* **116**, 9380–9389 (2019).
22. J. Oppermann *et al.*, MerMAIDs: A family of metagenomically discovered marine anion-conducting and intensely desensitizing channelrhodopsins. *Nat. Commun.* **10**, 1–13 (2019).
23. O. A. Sineshchekov *et al.*, Conductance mechanisms of rapidly desensitizing cation Channelrhodopsins from cryptophyte algae. *mBio* **11**, e00657-20 (2020).
24. B. K. Ho, F. Gruswitz, HOLLOW: Generating accurate representations of channel and interior surfaces in molecular structures. *BMC Struct. Biol.* **14**, 49 (2008).

25. V. A. Lórenz-Fonfría *et al.*, Temporal evolution of helix hydration in a light-gated ion channel correlates with ion conductance. *Proc. Natl. Acad. Sci. U.S.A.* **112**, E5796–E5804 (2015).
26. E. Ritter, K. Stehfest, A. Berndt, P. Hegemann, F. J. Bartl, Monitoring Light-induced Structural Changes of Channelrhodopsin-2 by UV-visible and Fourier Transform Infrared Spectroscopy. *J. Biol. Chem.* **283**, 35033–35041 (2008), https://doi.org/10.1074/jbc.m806353200.
27. I. Radu *et al.*, Conformational Changes of Channelrhodopsin-2. *J. Am. Chem. Soc.* **131**, 7313–7319 (2009), https://doi.org/10.1021/ja8084274.
28. S. Ito *et al.*, Water-containing hydrogen-bonding network in the active center of Channelrhodopsin. *J. Am. Chem. Soc.* **136**, 3475–3482 (2014).
29. J. I. Ogren *et al.*, Retinal chromophore structure and schiff base interactions in red-shifted channelrhodopsin-1 from *chlamydomonas augustae*. *Biochemistry* **53**, 3961–3970 (2014).
30. S. Bruun *et al.*, Light-dark adaptation of channelrhodopsin involves photoconversion between the all- trans and 13- cis retinal isomers. *Biochemistry* **54**, 5389–5400 (2015).
31. J. Kuhne *et al.*, Early formation of the ion-conducting pore in channelrhodopsin-2. *Angew. Chem. (Int. Ed.)* **54**, 4953–4957 (2015).
32. M. S. Braiman, O. Bousché, K. J. Rothschild, Protein dynamics in the bacteriorhodopsin photocycle: Submillisecond Fourier transform infrared spectra of the L, M, and N photointermediates. *Proc. Natl. Acad. Sci. U.S.A.* **88**, 2388–2392 (1991).
33. F. M. Hendrickson, F. Burkard, R. M. Glaeser, Structural characterization of the L-to-M transition of the bacteriorhodopsin photocycle. *Biophys. J.* **75**, 1446–1454 (1998).
34. A. K. Dioumaev *et al.*, Proton transfers in the photochemical reaction cycle of proteorhodopsin. *Biochemistry* **41**, 5348–5358 (2002).
35. T. Friedrich *et al.*, Proteorhodopsin is a light-driven proton pump with variable vectoriality. *J. Mol. Biol.* **321**, 821–838 (2002).
36. Y. Xiao, R. Partha, R. Krebs, M. Braiman, Time-resolved FTIR spectroscopy of the photointermediates involved in fast transient H^+ release by Proteorhodopsin. *J. Phys. Chem. B* **109**, 634–641 (2005).
37. E. C. Saint Clair, J. I. Ogren, S. Mamaev, J. M. Kralj, K. J. Rothschild, Conformational changes in the archaerhodopsin-3 proton pump: Detection of conserved strongly hydrogen bonded water networks. *J. Biol. Phys.* **38**, 153–168 (2012).
38. B. Nie, J. Stutzman, A. Xie, A vibrational spectral maker for probing the hydrogen-bonding status of protonated Asp and Glu residues. *Biophys. J.* **88**, 2833–2847 (2005).
39. D. Goyer, M. T. Roberts, Long-range Channelrhodopsin-assisted circuit mapping of inferior colliculus neurons with blue and red-shifted Channelrhodopsins. *JoVE* **156**, 60760 (2020).
40. D. J. Rindner, G. Lur, Practical considerations in an era of multicolor optogenetics. *Front. Cell. Neurosci.* **24**, 1160245 (2023).
41. J. C. D. Kaufmann *et al.*, Proton transfer reactions in the red light-activatable channelrhodopsin variant ReaChR and their relevance for its function. *J. Biol. Chem.* **292**, 14205–14216 (2017).
42. Y. Hontani *et al.*, Reaction dynamics of the chimeric channelrhodopsin C1C2. *Sci. Rep.* **7**, 7217 (2017).
43. O. A. Sineshchekov, E. G. Govorunova, J. Wang, H. Li, J. L. Spudich, Intramolecular proton transfer in channelrhodopsins. *Biophys. J.* **104**, 807–817 (2013).
44. H. Li, E. G. Govorunova, O. A. Sineshchekov, J. L. Spudich, Role of a helix B lysine residue in the photoactive site in channelrhodopsins. *Biophys. J.* **106**, 1607–1617 (2014).
45. T. Dudev *et al.*, Selectivity mechanism of the voltage-gated proton channel, HV1. *Sci. Rep.* **5**, 10320 (2015).
46. J. Tittor, D. Oesterhelt, The quantum yield of bacteriorhodopsin. *FEBS Lett.* **263**, 269–273 (1990).
47. E. Ritter, P. Piwowarski, P. Hegemann, F. J. Bartl, Light-dark adaptation of Channelrhodopsin C128T mutant. *J. Biol. Chem.* **288**, 10451–10458 (2013).
48. W. Sperling, P. Carl, C. Rafferty, N. A. Dencher, Photochemistry and dark equilibrium of retinal isomers and bacteriorhodopsin isomers. *Biophys. Struct. Mech.* **3**, 79–94 (1977).
49. C. Gergely, C. Ganea, G. Váró, Combined optical and photoelectric study of the photocycle of 13-cis bacteriorhodopsin. *Biophys. J.* **67**, 855–861 (1994).
50. A. Kawanabe, H. Kandori, Photoreactions and structural changes of *Anabaena* sensory rhodopsin. *Sensors (Basel)* **9**, 9741–9804 (2009).
51. M. P. Chien *et al.*, Photoactivated voltage imaging in tissue with an archaerhodopsin-derived reporter. *Sci Adv.* **7**, eabe3216 (2021).
52. E. Govorunova *et al.*, RubyACRs, non-algal anion channelrhodopsins with highly red-shifted absorption. *Proc. Natl. Acad. Sci. U.S.A.* **117**, 22833–22840 (2020).
53. O. A. Sineshchekov, E. G. Govorunova, H. Li, Y. Wang, J. L. Spudich, Sequential absorption of two photons creates a bistable form of RubyACR responsible for its strong desensitization. *Proc. Natl. Acad. Sci. U.S.A.* **120**, e2301521120 (2023).
54. A. Silapetere *et al.*, QuasAr Odyssey: The origin of fluorescence and its voltage sensitivity in microbial rhodopsins. *Nat. Commun.* **13**, 5501 (2022).
55. A. Rozenberg, K. Inoue, H. Kandori, O. Béjà, Microbial rhodopsins: The last two decades. *Annu. Rev. Microbiol.* **75**, 427–447 (2021).
56. E. G. Govorunova *et al.*, Kalium channelrhodopsins are natural light-gated potassium channels that mediate optogenetic inhibition. *Nat. Neurosci.* **25**, 967–974 (2022).
57. M. Nagase *et al.*, All-optical presynaptic plasticity induction by photoactivated adenylyl cyclase targeted to axon terminals. *Cell Rep. Methods* **4**, 100740 (2024).
58. R. Chen *et al.*, Deep brain optogenetics without intracranial surgery. *Nat. Biotechnol.* **39**, 161–164 (2021).
59. J. Bauer *et al.*, Limited functional convergence of eye-specific inputs in the retinogeniculate pathway of the mouse. *Neuron* **109**, 2457–2468.e12 (2021).
60. A. Mark Cigan, T. F. Donahue, Sequence and structural features associated with translational initiator regions in yeast – a review. *Gene* **59**, 1–18 (1987), https://doi.org/10.1016/0378-1119(87)90261-7.
61. C. Grimm, J. Vierock, P. Hegemann, J. Wietek, Whole-cell patch-clamp recordings for electrophysiological determination of ion selectivity in Channelrhodopsins. *J. Vis. Exp.* **123**, 1–8 (2017).
62. C. Ruse *et al.*, Potassium-selective channelrhodopsins can exert hyper- or depolarizing effects in excitable cells of *Caenorhabditis elegans*, depending on experimental conditions. *Genetics* **230**, iyaf083 (2025).
63. C. Bamann, T. Kirsch, G. Nagel, E. Bamberg, Spectral characteristics of the photocycle of Channelrhodopsin-2 and its implication for channel function. *J. Mol. Biol.* **375**, 686–694 (2008).
64. S. Bruun *et al.*, The chromophore structure of the long-lived intermediate of the C128T channelrhodopsin-2 variant. *FEBS Lett.* **585**, 3998–4001 (2011).
65. M. Luck, P. Hegemann, The two parallel photocycles of the Chlamydomonas sensory photoreceptor histidine kinase rhodopsin 1. *J. Plant Physiol.* **217**, 77–84 (2017).
66. M. Elgeti, E. Ritter, F. J. Bartl, New insights into light-induced deactivation of active rhodopsin by SVD and global analysis of time-resolved UV/Vis- and FTIR-data. *Z. Phys. Chem.* **222**, 1117–1129 (2008).
67. E. R. Henry, J. Hofrichter, "Singular value decomposition: Application to analysis of experimental data" in *Methods in Enzymology, Numerical Computer Methods*, L. Brand, M. L. Johnson Eds. (Elsevier, 1992), vol. 210, pp. 129–192.
68. K. Nakazawa *et al.*, Requirement for hippocampal CA3 NMDA receptors in associative memory recall. *Science* **297**, 211–218 (2002).
69. L. Faiss *et al.*, Hippocampal commissural circuitry shows asymmetric cAMP-dependent synaptic plasticity. *ACS Chem. Neurosci.* **16**, 4236–4245 (2025).